International Journal of Nanomedicine

Dovepress
Taylor & Francis Group

Open Access Full Text Article

ORIGINAL RESEARCH

Targetable Biomimetic NIR-II Theranostic Nanoplatform for Highly Efficient Multimodal Imaging-Guided Photothermal Therapy of Cervical Cancer

Chenyang Chu[1,2,*], Zhong Du[3,*], Jing Wang[1,2], Maierhaba Aili[1,2], Jiaxing Li[4], Jiabao Xiong[3], Rong Ma[1,2], Cailing Ma[1,2], Nuernisha Alifu[5]

[1]Department of Gynecology, The First Affiliated Hospital of Xinjiang Medical University, State Key Laboratory of Pathogenesis, Prevention and Treatment of High Incidence Diseases in Central Asia, Urumqi, People's Republic of China; [2]Xinjiang Key Laboratory of Medical Animal Model Research, Xinjiang Medical University, Urumqi, People's Republic of China; [3]The Second Affiliated Hospital of Xinjiang Medical University, Xinjiang Medical University, Urumqi, People's Republic of China; [4]School of Medical Engineering and Technology, Xinjiang Medical University, Urumqi, People's Republic of China; [5]Science and Technology Innovation and Achievement Transformation Service Center, Xinjiang Medical University, Urumqi, People's Republic of China

*These authors contributed equally to this work

Correspondence: Cailing Ma, Department of Gynecology, The First Affiliated Hospital of Xinjiang Medical University, State Key Laboratory of Pathogenesis, Prevention and Treatment of High Incidence Diseases in Central Asia, Urumqi, 830054, People's Republic of China, Email hymcl@sina.com; Nuernisha Alifu, Science and Technology Innovation and Achievement Transformation Service Center, Xinjiang Medical University, Urumqi, 830011, People's Republic of China, Email nens_xjmu@126.com

Purpose: Cervical cancer (CC) is still the fourth most common cause of cancer deaths in women. However, current biomedical imaging techniques exhibit inherent limitations in the diagnosis and treatment of CC. This study aims to develop a biomimetic nanoplatform based on tumor cell membranes, loaded with a palladium (Pd)-based computed tomography (CT) contrast agent and the near-infrared (NIR) fluorescent probe indocyanine green (ICG). This multifunctional nanoplatform is designed to integrate multimodal imaging with photothermal therapy (PTT), thereby improving the diagnostic accuracy and therapeutic efficacy against CC.

Methods: In this study, biomimetic nanoparticles (NPs), designated as M@Pd-ICG NPs, were synthesized by encapsulating Pd and ICG within HeLa cell membranes derived from cell-derived xenograft (CDX) models. Subsequently, the toxicity, biocompatibility, and tumor suppression capability of the M@Pd-ICG NPs were evaluated in vitro. In vivo, the multimodal imaging performance of the M@Pd-ICG NPs and their photothermal therapeutic efficacy under 808-nm laser irradiation were investigated in mouse model bearing subcutaneous cervical tumor.

Results: The M@Pd-ICG NPs were successfully prepared and exhibited favorable stability, excellent photothermal conversion efficiency (34.04%), and good biocompatibility, enabling homologous targeting and prolonged circulation time. The M@Pd-ICG NPs integrated the complementary advantages of NIR-II fluorescence imaging (900–1700 nm, NIR-II FI), photothermal imaging (PTI), and CT imaging. Both in vitro and in vivo studies demonstrated that, under 808-nm laser irradiation, M@Pd-ICG NPs induced significant photothermal effects and tumor ablation.

Conclusion: M@Pd-ICG NPs successfully integrate multimodal imaging and PTT, owing to their excellent targeting capability and good biocompatibility, demonstrating potential for further biomedical applications.

Keywords: cervical cancer, tumor cell membranes, palladium, indocyanine green, multimodal imaging, photothermal therapy

Introduction

Cervical cancer (CC) ranks as the fourth most common cancer among women worldwide.[1] Although its incidence has declined markedly over the past three decades, it remains a major global public health challenge with pronounced

https://doi.org/10.2147/IJN.S576589
Received: 8 November 2025
Accepted: 11 March 2026
Published: 27 March 2026

regional disparities in both incidence and mortality.[2–4] Diagnostic imaging plays a pivotal role in the initial assessment, staging, evaluation of treatment efficacy and surveillance for recurrence of CC. Ultrasonography is cost-effective, noninvasive, and readily accessible at the bedside, but its sensitivity to deep tissue invasion and lymph node assessment is limited.[5] Magnetic resonance imaging (MRI) offers superior soft tissue resolution and enables quantitative tumor characterization via diffusion-weighted imaging (DWI) and dynamic contrast-enhanced (DCE) sequences, yet it still suffers from prolonged scan times and contraindications.[6,7] Computed tomography (CT) provides rapid imaging with widespread availability, leveraging the deep penetration and high spatial resolution of X-rays, which delivers three-dimensional macroscopic localization and quantitative evaluation of tumors and surrounding anatomical structures. However, CT is constrained by suboptimal soft tissue contrast, limited sensitivity for minute lesions, and inherent radiation risks.[8,9] Therefore, novel imaging technology with enhanced sensitivity and improved accuracy is in great demand for precise diagnosis and treatment.

Advances in nanotechnology have promoted effective and comprehensive novel diagnostic techniques. Near-infrared fluorescence imaging (NIRFI) is a promising optical imaging technology operating in the near-infrared (NIR, 700–-1700nm) spectrum with advantages of non-invasive property, high molecular sensitivity and real-time dynamic monitoring with assistance of fluorescent dyes irradiated with NIR lasers.[10] Additionally, photothermal imaging (PTI), under NIR irradiation, is an attractive imaging modality, which could noninvasively and continuously monitor temperature changes within the tumor region, directly providing feedback on photothermal effect.[11] Nevertheless, both NIRFI and PTI are hindered by shallow tissue penetration and inadequate anatomical details.[12] Thus, combining NIRFI, PTI with CT imaging could help to achieve super penetration depth and high resolution/sensitivity as well as accurate temperature progress which could fulfill quick tumor localization with high accuracy is of great importance.

With the advancement of nanomedicine, various multifunctional nanomaterials have been designed and engineered. Among them, NIR theranostic nanoprobes have garnered significant attention for their diagnostic and therapeutic potential. In particular, ICG is considered an ideal candidate due to its NIR fluorescence and PTT property, which has received Food and Drug Administration (FDA) approval.[13] However, ICG suffers from inherent limitations, including poor stability and rapid blood circulation, which restrict its further application. To address these limitations, encapsulating ICG within liposomes has been demonstrated to enhance its photostability, thereby improving its applicability in NIRFI.[14,15] Additionally, the liposomal framework offers a versatile platform for integrating metallic nanoparticles (NPs) with therapeutic or imaging agents, enabling synergistic theranostic functions and enhancing stability.[16] Compared to other metallic nanomaterials, Pd-based nanomaterials exhibit superior photostability and photothermal conversion efficiency in the NIR region, rendering palladium NPs (Pd NPs) a highly attractive alternative to conventional photothermal agents for noninvasive cancer therapy.[17,18] Pd possesses a relatively high atomic number and metal density, which results in a great number of electrons per unit volume participating in X-ray attenuation, thereby enabling Pd to exhibit a pronounced photoelectric absorption effect within the conventional energy range of X-ray scanning, and consequently improving imaging performance.[8,19] However, like other metallic nanomaterials, Pd-based nanomaterials face challenges related to biocompatibility and targeting specificity.

To enhance biosafety and targeting capacity, a biomimetic approach, utilizing tumor cell membranes derived from cell-derived xenograft (CDX) model, offers a promising strategy.[20] The core mechanism by which tumor cell membranes achieve homologous targeting lies in their retention of the specific protein molecules present on the surface of the original tumor cells. These molecules not only endow the NPs with immune evasion and prolonged circulation, but also facilitate active homologous uptake by tumor cells.[21,22] Early studies in this field have demonstrated that tumor cell membrane-coated NPs exhibit 40-fold and 20-fold higher tumor cell uptake efficiency compared to erythrocyte membrane-coated NPs and uncoated NPs, respectively.[23] Notably, tumor cell membranes coating significantly enhances stability of NPs, further improving blood circulation and tumor accumulation.[24] This strategy leverages the intrinsic homologous targeting properties of tumor cell membranes to develop a versatile nanoplatform for multimodal imaging and photothermal therapy (PTT), establishing a robust foundation for precision tumor diagnosis and treatment.

In this study, a new biomimetic theranostic nanoplatform, M@Pd-ICG nanoparticles (MPI NPs), was designed and synthesized, via coating Pd NPs and ICG within liposomes and cloaking them with CDX-derived HeLa cell membranes. This design confers homologous tumor targeting and immune evasion, and integrates multimodal imaging, including

NIRFI, PTI, and CT imaging, to achieve synergistic theranostic functions. While maintaining excellent biosafety in vivo, MPI NPs exhibited remarkable photothermal conversion efficiency under NIR 808-nm laser irradiation, enabling precise and efficient tumor ablation (Scheme 1). Compared to previous single agent nanotheranostic systems based solely on ICG or Pd, this study achieved homologous enrichment through tumor cell membranes camouflage and integrated NIRFI, PTI and CT imaging functions into a single nanoplatform, thereby realizing synergistic enhancements in terms of in vivo stability, multimodal cross-validation, and imaging-guided therapy.

Materials and Methods

Materials

The chemicals used in the experiments were of analytical grade and did not need further purification. The supplier of indocyanine green (ICG) was Shanghai Macklin Biochemical Co., Ltd. Palladium(II) acetylacetonate (Pd-$(acac)_2$),

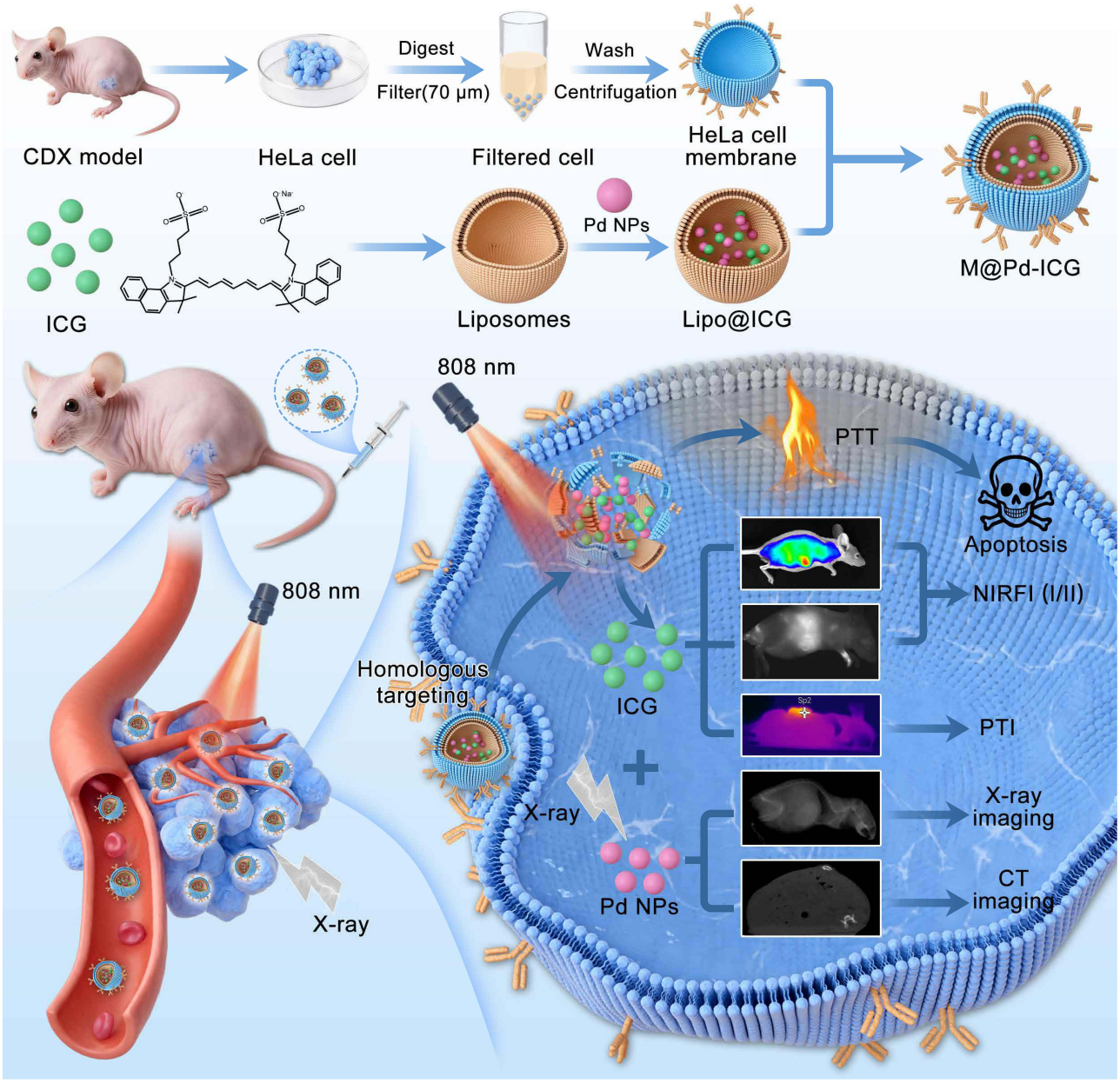

Scheme 1 Schematic diagram illustrating the synthesis process of MPI NPs and further application of multimodal imaging and PTT effect for in vivo cervical tumor.

https://doi.org/10.2147/IJN.S576589

cetyltrimethylammonium bromide (CTAB), N,N-dimethylformamide (DMF), L-ascorbic acid (L-AA), soybean phosphatidylcholine (SPC), DSPE-PEG_{2000} [1,2-distearoyl-sn-glycero-3-phosphoethanolamine-N-[methoxy (polyethylene glycol)-2000]], cholesterol, and chloroform were purchased from Shanghai Aladdin Biochemical Technology Co., Ltd. Phosphate-buffered saline (PBS), high-glucose DMEM, fetal bovine serum (FBS), and trypsin were sourced from Shanghai Gibco Co., Ltd. The PE Annexin V apoptosis detection kit was obtained from BD Biosciences Pharmingen Co., Ltd. Cell Counting Kit-8 (CCK-8), Hoechst 33342 staining solution, Coomassie Brilliant Blue staining solution, calcein AM, propidium iodide (PI),and TE buffer were obtained from Biosharp Co., Ltd. 4% paraformaldehyde, hematoxylin–eosin (H&E) staining solution, and EDTA anticoagulant tubes were purchased from Wilber Biotechnology Co., Ltd. The TUNEL apoptosis detection kit was obtained from Servicebio Co., Ltd. Isoflurane anesthetic was purchased from RWD Life Science Co., Ltd. All experiments were conducted using deionized water (DI water).

Cells and Animals

The HeLa human cervical cancer cell line, H8 human cervical epithelial cell line, and RAW 264.7 mouse macrophage cell line were acquired from the American Type Culture Collection (ATCC) and cultivated in DMEM medium enriched with 10% FBS and 1% penicillin-streptomycin (pen-strep) at 37 °C in a humidified incubator with 5% CO_2. Female BALB/c and nude mice (18–20 g) were obtained from Beijing Life River Laboratory and housed at Xinjiang Medical University's Animal Experiment Center.

The subcutaneous CC model was established by injecting 1×10^6 HeLa cells. Tumor volume (V) was calculated as $V = (L\times W^2)/2$, where L and W denote tumor length and width, respectively. The subcutaneous xenograft model was considered successfully established when tumor volume reached approximately 100 mm^3, at which point in vivo experiments were initiated.[25,26] All procedures were performed on mice under isoflurane inhalation anesthesia, and euthanasia was carried out by cervical dislocation at the end of the experiments. All animal treatment procedures were conducted in accordance with the American Veterinary Medical Association (AVMA) Guidelines for the Euthanasia of Animals. All animal husbandry management and experimental procedures were conducted in accordance with international regulations and animal welfare ethical requirements, with reference to the "Guide for the Care and Use of Laboratory Animals". All experimental protocols were approved by the Experimental Animal Ethics Committee of Xinjiang Medical University (Approval No.: IACUC-20220308-55) and the Animal Care and Use Committee (Approval No.: 20191113–08).

Preparation of CDX-Derived Tumor Cell Membranes

HeLa cells were cultured, digested, collected, and then resuspended in a DMEM/Matrigel suspension (approximately 1×10^7 cells/mL). Then, a 100 μL cell suspension was injected under the skin in the lateral abdominal area of BALB/c nude mice. Upon reaching the maximum tumor volume of 500 mm^3, the mice were euthanized, and tumor tissue was aseptically excised in a biosafety cabinet. The excised tumor was placed on ice in a 15 mL centrifuge tube containing sterile PBS, then transferred to a 10 cm culture dish using sterile forceps. The tumor was minced with a sterile scalpel, 10 mL of the solution for digestion was added, and the tissue fragments were gently mixed with the digestion solution by shaking the dish. The mixture underwent incubation at 37 °C in a 5% CO_2 environment for 15 min (the tissue volume should not exceed 1,500 mm^3 per 10 mL of digestion solution to ensure digestion efficiency). The mixture was triturated every 15 min and returned to the incubator until a homogeneous suspension was obtained (lasting ≤ 3 h). After digestion, the cell suspension was filtered using a 70 μm cell strainer placed on a 50 mL centrifuge tube and rinsed three times with saline solution. The cells were gathered by centrifugation at 1,000 rpm for 5 min, then resuspended in a hypotonic lysis buffer, and homogenized with 20 strokes using a Dounce homogenizer on ice.[27] The lysate underwent sequential centrifugation at 3,200 rpm for 10 min and 15,000 rpm for 30 min. The supernatant from the first spin was collected for the second spin; after the second spin, the pellet was rinsed with TE buffer containing 10 mM Tris-HCl and 1 mM EDTA, and recollected under the same conditions. The resulting pellet, representing purified HeLa cell membranes, was stored at −80 °C for subsequent use.[28]

Preparation of M@Pd-ICG NPs

M@Pd-ICG NPs were synthesized as follows. $Pd(acac)_2$ was added to 15 mL of DMF containing CTAB and the mixture was gradually heated to 90 °C in an oil bath under continuous stirring for 30 min. Subsequently, L-ascorbic acid (L-AA) was dissolved in 5 mL of DMF and then added to the reaction vessel, and stirring was maintained at 90 °C for an additional 60 min. The precipitate was harvested by centrifugation at 12,000 rpm, washed with a mixture of ethanol and water, and redispersed in water to obtain Pd NPs.[29,30] SPC, DSPE-PEG_{2000}, cholesterol, and ICG were dissolved in 3 mL of chloroform and added to a sample vial. A thin film was formed by rotary evaporation under reduced pressure. The aqueous dispersion of Pd NPs was then added to hydrate the film, and the mixture was sonicated and extruded through a liposome extruder equipped with a polycarbonate membrane to form lipid-coated Pd-ICG NPs (Lipo@Pd-ICG NPs).[31,32] The resulting suspension was dialyzed and brought with DI water to a final volume of 2 mL. Finally, extracted HeLa cell membranes were introduced, after pre-mixing under ice-bath conditions, the mixture was co-extruded through a polycarbonate membrane to obtain HeLa cell membrane-coated Pd NPs and ICG (M@Pd-ICG NPs).[33]

Characterization of M@Pd-ICG NPs

The morphological characteristics of MPI NPs were investigated via transmission electron microscopy (TEM; JEOL JEM-F200, Japan). The protein profiles of MPI NPs and HeLa cell membranes were compared by sodium dodecyl sulfate-polyacrylamide gel electrophoresis (SDS-PAGE) followed by Coomassie Brilliant Blue staining and imaged on a multimode system (Azure Biosystems 600). The energy-dispersive X-ray spectroscopy was performed (EDS, JSM-7610F Plus). The chemical composition and valence states of MPI NPs were characterized by Fourier transform spectroscopy (FT-IR) and X-ray photoelectron spectroscopy (XPS; ESCALAB 250Xi, Thermo Scientific). The hydrodynamic diameter and zeta potential of MPI NPs were measured with a Malvern NP size analyzer (ZS90, UK). The absorption spectra of ICG, and MPI NPs were obtained from a Shimadzu UV-3600 Plus instrument, and the fluorescence spectra of ICG, and MPI NPs were determined via a Duetta fluorescence and absorbance spectrofluorophotometer (HORIBA Scientific, Canada).

The drug loading capacity (DLC) and encapsulation efficiency (EE) of ICG were determined by UV-Vis spectrophotometry. The ICG loading in MPI NPs was quantified from absorbance measurements. DLC and EE were computed using the following equations:[34]

$$DLC(\%) = \frac{W_{ICG}}{W_{M@Pd-ICG}} \times 100\%$$

$$EE(\%) = \frac{W_{ICG}}{W_{T-ICG}} \times 100\%$$

In vitro Evaluation of Photothermal Performance

The photothermal properties of MPI NPs in aqueous dispersion were evaluated. To comprehensively evaluate the photothermal performance of MPI NPs, the temperature rise of aqueous dispersion of MPI NPs at four concentrations (40, 60, 80, and 100 μg mL^{-1}) was monitored under 808-nm laser irradiation (1.0 W cm^{-2}). Similarly, the heating behavior of MPI NPs dispersion at a fixed concentration (80 μg mL^{-1}) was further examined under four different laser power densities (0.6, 0.8, 1.0, and 1.2 W cm^{-2}). To benchmark against controls, PBS, free ICG, Pd NPs, and MPI NPs dispersion were irradiated with an 808-nm laser (1.0 W cm^{-2}) for 15 min, and the corresponding temperature changes were measured. The photothermal stability of the 80 μg mL^{-1} MPI NPs dispersion was evaluated over five consecutive heating–cooling cycles, and the resulting stability curve was plotted. The temperature variations for each sample were monitored at fixed time intervals with an infrared thermal camera (FOTRIC 323 Pro), and the photothermal conversion efficiency (η) was computed using the following equation:[35]

$$\eta = \frac{M_D C_D \left(T_{max} - T_{\max,water}\right)}{\tau s \left(1 - 10^{-A808}\right)} \times 100\%$$

https://doi.org/10.2147/IJN.S576589

(M_D) and (C_D) denote the mass and heat capacity of DI water, T_{max} and $T_{max,\ water}$ represent the maximum equilibrium temperatures of NPs solution and water, τ_s is the system time constant, I is the NIR laser power, and A_{808} is the dispersion absorbance at 808-nm.

Cytotoxicity Analysis

Cell viability was assessed using the CCK-8 assay. Dark toxicity: HeLa cells (5×10^3 cells per well) were seeded in 96-well plates and cultured for 24 h. MPI NPs were then added at varying concentrations (10, 20, 40, 60, 80, 100, and 200 μg mL^{-1}) and co-incubated for 6–8 h. Then, 10 μL of CCK-8 reagent was added to each well and cultured in the dark for 2–4 h. The optical density (OD) value was measured at 450 nm using a microplate reader. Phototoxicity: HeLa cells (5×10^3 cells per well) were seeded and cultured as above. MPI NPs were added at the same concentration range and incubated for 6–8 h. Then, cells were irradiated with an 808-nm laser (1.0 W cm^{-2}, 10 min), followed by the addition of 10 μL CCK-8 reagent per well and incubation in the dark for 2–4 h. The OD value was measured at 450 nm by a microplate reader. The OD value of control wells was monitored at set intervals to ensure they remained near 1.0. Cell viability was evaluated by normalizing the OD of the intervention group to that of the control, as follows:[36]

$$CellViability(\%) = \frac{OD_{intervention} - OD_{blank}}{OD_{control} - OD_{blank}} \times 100\%$$

The $OD_{intervention}$, $OD_{control}$ and OD_{blank} correspond to the intervention, control and blank groups, respectively. Each experiment was repeated at least three times, and cell viability is recorded as mean ± standard deviation.

Cellular Uptake

Confocal laser scanning microscopy (CLSM) was employed for cell imaging. 1×10^5 HeLa cells were seeded into glass-bottom culture dishes (35 mm in diameter) and cultured for 24 h. Cells were then incubated in complete medium supplemented with either free ICG or MPI NPs for 2 h. After medium removal, cells were washed three times with PBS and stained with Hoechst 33342 for 10 min, and rinsed three additional times with PBS. Fluorescence images were acquired using a CLSM (Zeiss LSM 900, Germany). To compare the uptake efficiency of MPI NPs among different cell types, 1×10^5 HeLa, H8, and RAW 264.7 cells were seeded into confocal culture dishes and incubated with MPI NPs in complete medium for 2 h. After Hoechst 33342 staining, images were captured by CLSM.

For quantitative analysis of ICG and MPI NPs uptake by HeLa cells, three parallel 6-well plate experiments were conducted, with 3×10^5 HeLa cells per well cultured for 24 h. Cells were treated with free ICG or MPI NPs for 2 h, then washed with PBS, trypsinized, and collected by centrifugation. Pelleted cells were washed twice with PBS, resuspended in 500 μL of 1×Annexin binding buffer, and analyzed by flow cytometry (BD LSR II, BD Biosciences) to quantify ICG fluorescence.

In vitro Evaluation of Photothermal Effect

To evaluate the photothermal effect of MPI NPs on HeLa cells, four experimental groups were established. First, 4×10^5 HeLa cells were seeded into four confocal culture dishes (1×10^5 cells per dish) and cultured for 24 h before grouping: control group, laser-only group, MPI NPs group, and MPI NPs + laser group. The control group received no treatment. The laser-only group was irradiated with 808-nm laser irradiation (1.0 W cm^{-2}) for 10 min. The MPI NPs group was incubated with 80 μg mL^{-1} MPI NPs for 2 h. The MPI NPs + laser group was incubated with 80 μg mL^{-1} MPI NPs for 2 h, followed by 808-nm laser irradiation (1.0 W cm^{-2}, 10 min). After treatment, all groups were dual-stained with Calcein-AM and PI, and subsequently observed under CLSM. Fluorescence images were acquired at excitation wavelengths of 490 nm (Calcein-AM, green) and 545 nm (PI, red), with emission detected in the 810–1000 nm range.

For quantitative analysis of the in vitro photothermal effect, a parallel experiment was conducted using six-well plates, with 3×10^5 HeLa cells per well. After 24 h of culture, the cells were grouped and treated following the same protocol as described above. Post-treatment, cells were washed with 1× PBS, trypsinized, and collected by centrifugation. The harvested cells were washed twice with 1× PBS, resuspended in 500 μL of 1× Annexin binding buffer, and stained with 5 μL 7-AAD and 5 μL PE Annexin V. After gentle vortexing, the samples were incubated in the dark for 15 min and then analyzed by flow cytometer.

In vivo Metabolic and Biosafety Evaluation

To evaluate the distribution of MPI NPs in normal living organisms, nude mice were injected via the tail vein with MPI NPs (1 mg kg^{-1}) or PBS (control). The fluorescence distribution of MPI NPs in mice was monitored at different time points (2, 8, 24, and 48 h) using a small-animal IVIS Spectrum in vivo Imaging System. After 48 h, animals were euthanized, and major organs (heart, liver, spleen, lungs, kidneys) were harvested for ex vivo fluorescence analysis to determine the distribution profile of MPI NPs in healthy mice.

The heparinized tubes were used to collect whole blood specimens from healthy BALB/c mice, and red blood cells (RBCs) were separated by centrifugation at 2700 rpm for 15 min. After serum removal, serum was removed, and the RBCs suspension was obtained via three sequential PBS rinses. The RBCs suspension was incubated with physiological saline containing MPI NPs at concentrations of 10, 20, 40, 60, 80, 100, and 200 μg mL^{-1} at 37 °C for 2 h. DI water and saline served as positive and negative controls, respectively. Subsequently, 100 μL of supernatant was transferred to a 96-well plate, and OD value was measured at 545 nm using a microplate reader. The degree of hemolysis was calculated from hemoglobin release:

$$HemolysisRate(\%) = \frac{OD_{sample} - OD_{negative}}{OD_{positive} - OD_{negative}} \times 100\%$$

For comprehensive biosafety evaluation, BALB/c mice were randomized into four groups (n = 3 per group). Three groups were injected with MPI NPs (1 mg kg^{-1}) and sacrificed at 1, 7, and 14 days post-injection, respectively, while the control group received PBS and was sacrificed on Day 14. Blood was collected from the retro-orbital venous plexus for routine hematological and serum biochemical analysis, and major organs were excised for H&E histopathology.

In vivo Multimodal Imaging

The experimental design for assessing the tumor-targeting ability of MPI NPs in vivo. Four groups of CC-bearing mouse models were established. Two groups were administered PBS via tail vein injection, while the other two groups received MPI NPs (1 mg kg^{-1}). And then, fluorescence signals in mice were dynamically monitored at 2, 8, 24, and 48 h post-injection using a small-animal IVIS Spectrum Imaging System (PerkinElmer, USA) and an NIR-II IVIS Imaging System (MARS-Pathfinder). After 48 h, mice were euthanized, and the hearts, livers, spleens, lungs, kidneys, and tumor tissues were excised for ex vivo fluorescence imaging. In an additional experimental group, simultaneous observation of NIR-I fluorescence signals and X-ray imaging was conducted 24 h after tail vein injection of MPI NPs. Quantification of Pd concentrations in different organs was performed by inductively coupled plasma mass spectrometry (ICP-MS) at the Xinjiang Institute of Ecology and Geography, Chinese Academy of Sciences. Finally, the in vitro and in vivo imaging performance of MPI NPs was evaluated using a micro-CT imaging system (Xradia 515 Versa, ZEISS, Germany).

In vivo PTT Performance

To evaluate the in vivo targeted photothermal properties and PTT efficacy of MPI NPs, a subcutaneous CC xenograft model was established in nude mice. Two groups of tumor-bearing nude mice were employed for in vivo photothermal evaluation: the experimental group received MPI NPs (1 mg kg^{-1}) via tail vein injection, while the control group was administered 50 μL of 1×PBS. After 24 h, both groups were subjected to 808-nm laser irradiation (1.0 W cm^{-2}, 10 min), and temperature changes in the subcutaneous tumor regions were recorded using an infrared thermal imaging system.

Subsequently, 16 tumor-bearing nude mice were randomly assigned to four groups (n = 4 per group) for in vivo PTT evaluation: (1) control group; (2) laser-only group; (3) MPI NPs group; and (4) MPI NPs + laser group. The laser-only group received 808-nm laser irradiation (1.0 W cm^{-2}) for 10 min at the tumor site. The MPI NPs group was administered MPI NPs at a dose of 1 mg kg^{-1} by tail-vein injection. The combination treatment group received laser irradiation 24 h post-injection under the same parameters. Tumor volume changes and body weight fluctuations were monitored at regular intervals throughout the experiment. After 15 days, the mice were euthanized, and major organs (heart, liver, spleen, lung, and kidney) along with tumor tissues were collected. Tumor tissues were weighed to assess therapeutic efficacy, and then fixed for H&E staining. Histological evaluation was performed on H&E sections using an inverted fluorescence microscope (TS2R-FL, Nikon).

TUNEL staining was performed on tumor tissue sections to assess DNA fragmentation. Tumor sections were deparaffinized, rehydrated, and then washed in PBS. Slides were subsequently incubated with proteinase K (20 μg mL^{-1}, 20 min), followed by PBS washing. Next, sections were equilibrated in buffer for 20 min, and incubated with terminal deoxynucleotidyl transferase (TdT) reaction mix at 37 °C for 1 h in the dark. Following two PBS washes, nuclei were counterstained with DAPI (5 min), rinsed, and imaged immediately by fluorescence microscopy.

Statistical Analysis

All experimental data collected were expressed as mean ± standard deviation (SD). Statistical significance was evaluated by one-way ANOVA, with significance thresholds of *$p < 0.05$, **$p < 0.01$, and ***$p < 0.001$. Statistical analyses were performed in GraphPad Prism v10.41. Flow cytometry data were processed with FlowJo v10.9.0, and fluorescence grayscale images were analyzed in ImageJ.

Results and Discussion

A biomimetic nanoplatform was engineered using cancer cell membranes derived from CDX model to enable synergistic multimodal imaging and PTT. The core consists of liposome-encapsulated NIR fluorescent dye ICG and CT contrast enhancer Pd NPs, while the outer shell is composed of CDX-derived HeLa cell membranes. MPI NPs integrate CT, NIRFL, and PTI modalities to provide complementary multimodal imaging. The CDX-derived HeLa cell membranes coating not only confers immune evasion and prolonged circulation, but also enables precise tumor targeting through homologous adhesion proteins. Under 808-nm laser irradiation, ICG and Pd NPs synergistically induce precise tumor ablation via PTT (Scheme 1). This integrated strategy holds significant promise for the diagnosis and treatment of CC.

Synthesis and Characterization of M@Pd-ICG NPs

Pd NPs were synthesized via redox reaction with $Pd(acac)_2$ (Figure 1A). Subsequently, Lipo@Pd-ICG were cloaked with CDX-derived HeLa cell membranes through ultrasonication, successfully yielding M@Pd-ICG (MPI) NPs (Figure 1B). Both Pd NPs and MPI NPs observed under TEM exhibited uniform spherical morphology. As shown in Figure 1C, the EDS detected the presence of C, P, S, and Pd elements. Moreover, the uniform distribution of these elements within the NPs indicates the successful preparation of MPI NPs. To verify successful HeLa cell membranes modification, membrane protein composition was analyzed by SDS-PAGE with Coomassie Brilliant Blue staining.[37] Figure 1D demonstrates distinct protein bands from extracted membrane proteins, visually confirming successful coating of tumor cell membranes on the surfaces of the NPs.

MPI NPs were further characterized to verify their structure and composition. As illustrated in Figure 1E, free ICG exhibited a characteristic absorption peak at 780 nm, while the absorption peak of MPI NPs was slightly shifted to 805 nm, attributed to interactions with phospholipids and membrane proteins. Fluorescence spectra (Figure 1F) of free ICG and MPI NPs revealed that the fluorescence peak of free ICG occurred at 804 nm, while MPI NPs was at 853 nm. The slight red shift of the fluorescence emission peak of MPI NPs may be attributed to lipid-mediated modification that promoted the transition of ICG from a monomeric to an aggregated state within cell membranes, resulting in changes to the charge density distribution of intermolecular interactions.[38,39] The EDS spectra (Figure 1G) showed characteristic peaks attributable to C, P, S, and Pd, and the XPS spectra (Figure 1H) further confirmed their chemical states. The full survey spectrum exhibited the presence of C, O, P, S, and Pd elements. The Pd 3d XPS spectrum (Figure S1) revealed peaks at 337.16 eV and 342.26 eV, corresponding to Pd^0 $3d_{5/2}$ and $3d_{3/2}$ orbitals, indicating that Pd is predominantly metallic form (Pd^0).[40] Furthermore, in the FTIR spectra (Figure 1I), the characteristic aromatic ring skeleton vibrations of ICG (1536 cm^{-1}, 1504 cm^{-1}) appeared simultaneously with the characteristic peaks of the phospholipid framework and proteins of the cell membranes (1739 cm^{-1}, 1087 cm^{-1}). This observation confirmed, at the molecular level, the successful encapsulation of Pd and ICG within the biomimetic membrane. The slight shifts in the molecular energy levels were attributed to interactions between the components.

Subsequently, MPI NPs underwent comprehensive physicochemical characterization. DLS measured the average hydrodynamic diameter of ~150 nm for MPI NPs (Figure 1J). Absorption spectroscopy quantified DLC as 25.0% (Pd NPs) and 1.3% (ICG), with EE of 96.1% and 98.4%, respectively. As depicted in Figure 1K, zeta-potential analysis

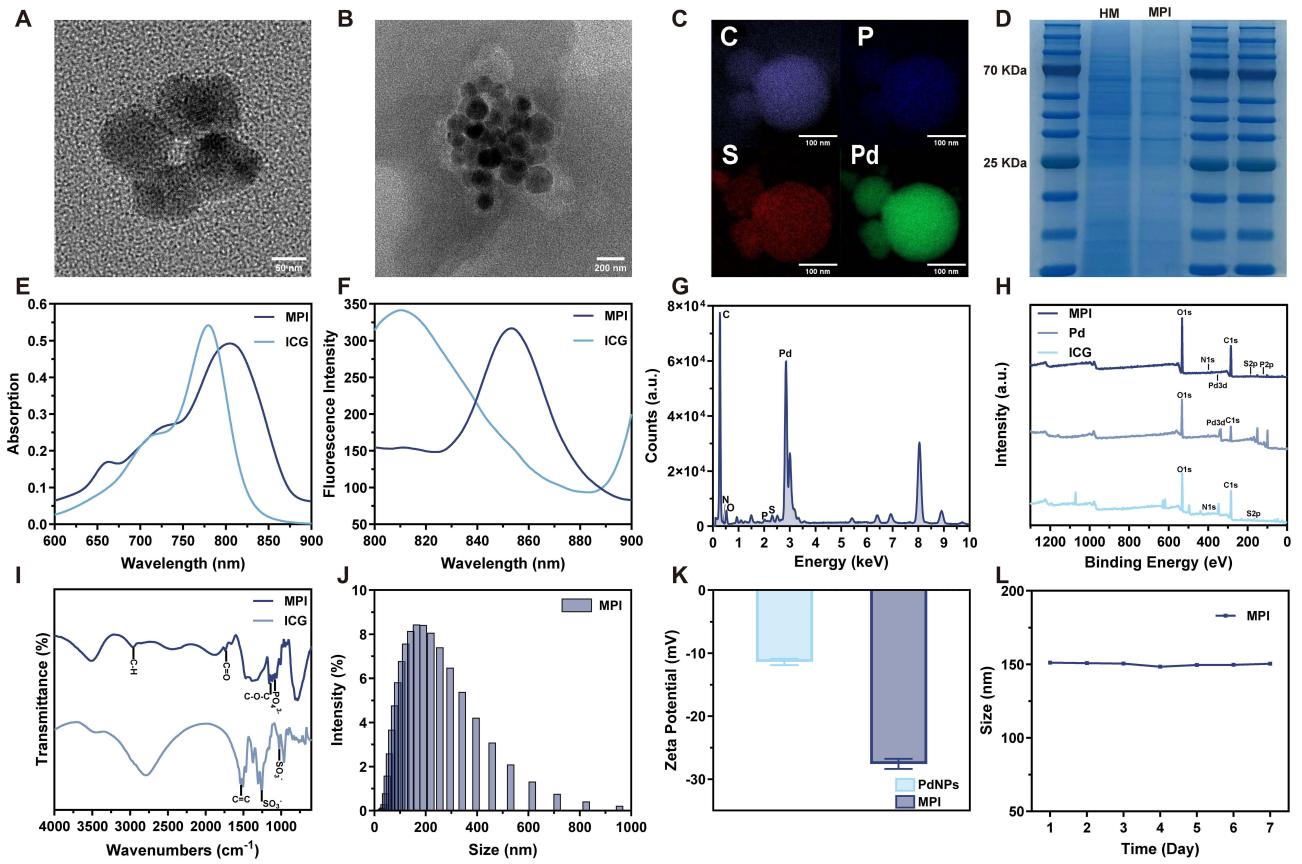

Figure 1 Preparation and characterization of MPI NPs. (**A**) TEM image of Pd NPs. (**B**) TEM image of MPI NPs. (**C**) Elemental mapping of MPI NPs. (**D**) Membrane protein analysis of HeLa cell membranes and MPI NPs. (**E**) Absorption spectra of free ICG and MPI NPs. (**F**) Fluorescence spectra of free ICG and MPI NPs. (**G**) EDS spectrum of MPI NPs. (**H**) High-resolution full XPS spectrum of MPI NPs. (**I**) FT-IR of free ICG and MPI NPs. (**J**) DLS analysis of MPI NPs. (**K**) Zeta potential of Pd NPs and MPI NPs. (**L**) Particle size stability of MPI NPs in aqueous solution for 1–7 days.

provided additional evidence of successful HeLa cell membranes modification: the potential shifted from −11.37 mV (Pd NPs) to −27.59 mV (MPI NPs), consistent with successful membrane encapsulation. Additionally, stability experiments demonstrated that the average size and zeta potential of MPI NPs showed no appreciable changes over 7 days (Figures 1L and S2).

In vitro Evaluation of Photothermal Performance

According to the simulated Jablonski diagram, under 808-nm laser excitation, MPI NPs undergo direct radiative dissipation from the S_1 state to the S_0 state, emitting photons with lower energy and longer wavelength, which enables NIRFL. Additionally, the excited energy can also be dissipated via nonradiative vibrational relaxation to S_0, mediated by intramolecular motions and collisions with surrounding molecules, thereby generating heat generation and subsequently inducing PTT effect (Figure 2A).[41,42] The experiment of photobleaching resistance was assessed over 60 min using an NIR-II fluorescence microscopic imaging system, MPI NPs maintained high fluorescence signal intensity under continuous illumination (Figure 2B), demonstrating excellent photostability for prolonged imaging applications.

To evaluate in vitro photothermal performance, aqueous dispersion of MPI NPs at varying concentrations (40, 60, 80, and 100 μg mL^{-1}) were continuously irradiated with an 808-nm laser (1.0 W cm^{-2}). The results demonstrated that the photothermal efficacy of MPI NPs increased in a concentration-dependent manner (Figure 2C and D). Subsequently, temperature curves and corresponding NIR thermal images were acquired at laser power densities of 0.6, 0.8, 1.0, and 1.2 W cm^{-2} (Figure 2E and F). When the power density increased from 0.6 to 1.2 W cm^{-2}, the maximum temperature of the system reached 59.0 °C.

https://doi.org/10.2147/IJN.S576589

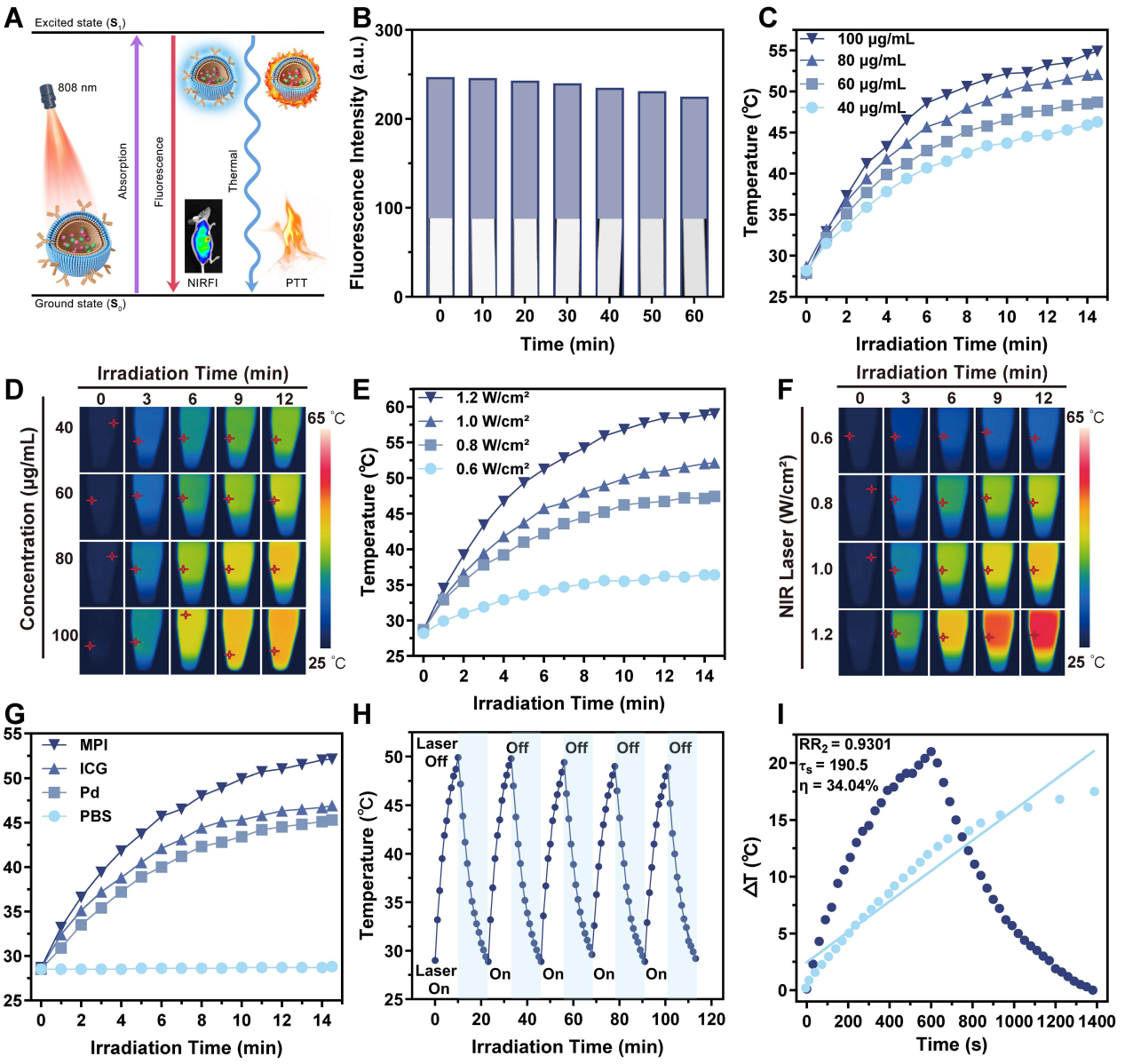

Figure 2 In vitro photothermal effect of MPI NPs. (**A**) Modified Jablonski diagram illustrating the PTT and NIRFI mechanisms of MPI NPs under 808-nm laser irradiation. (**B**) Fluorescence intensity analysis of MPI NPs (808-nm laser irradiation, 1 W cm^{-2}). (**C**) Temperature curves of MPI NPs in aqueous dispersion under 808-nm laser irradiation at different concentrations (40, 60, 80, 100 μg mL^{-1}) after 15 min at 1.0 W cm^{-2}. (**D**) NIR thermal imaging of MPI NPs at different concentrations under 808-nm laser irradiation (1.0 W cm^{-2}). (**E**) Temperature curves of MPI NPs aqueous solutions (80 μg mL^{-1}) under 808-nm laser irradiation at different power densities (0.6, 0.8, 1.0, 1.2 W cm^{-2}) for 15 min. (**F**) NIR thermal imaging of MPI NPs in aqueous dispersion (80 μg mL^{-1}) under 808-nm laser irradiation at different power densities. (**G**) Temperature curves of PBS, Pd NPs, ICG, and MPI NPs (80 μg mL^{-1}) under 808-nm laser irradiation at 1.0 W cm^{-2} for 15 min. (**H**) Photothermal stability curve of MPI NPs across five heating-cooling cycles (808 nm, 1.0 W cm^{-2}). (**I**) PCE of MPI NPs (80 μg mL^{-1}, 1.0 W cm^{-2}).

Subsequently, a systematic comparison was conducted between the photothermal properties of MPI NPs, ICG, Pd NPs, and PBS. As illustrated in Figure 2G, MPI NPs exhibited superior photothermal performance compared to individual ICG and Pd NPs, attributed to liposomal encapsulation and membrane cloaking. The cell membranes effectively aggregated free ICG and Pd NPs, while the liposomal encapsulation improved the photostability of ICG and its resistance to photobleaching.[43] This structural encapsulation not only enhanced thermal conductivity but also facilitated efficient heat transfer. Furthermore, Figure 2H demonstrated that the 80 μg mL^{-1} MPI NPs dispersion retained consistent temperature behavior over five heating-cooling cycles, demonstrating high photothermal stability. From the initial heating curve, photothermal conversion efficiency (PCE) was computed to be 34.04% (Figure 2I). The outstanding

https://doi.org/10.2147/IJN.S576589

photothermal performance and stability of MPI NPs provide a solid foundation for subsequent in vitro and in vivo experimental studies, highlighting their potential for applications in PTT.

In vitro Evaluation of Photothermal Therapy

As shown in Figure 3A, across concentrations up to 200 μg mL^{-1}, all groups maintained cell viability above 80% after 24 h incubation, indicating good biocompatibility of MPI NPs compared with Pd NPs and ICG. Under 808-nm laser irradiation, HeLa cells viability was reduced to below 20% in the 200 μg mL^{-1} MPI NPs group (Figure 3B), highlighting their photothermal therapeutic potential. By selecting the tumor cell membranes as carrier for the NPs, the metallic toxicity of Pd NPs was effectively mitigated, and the stability of ICG was enhanced, laying the groundwork for subsequent in vivo studies. Considering both biotoxicity and therapeutic efficacy, the concentration of 80 μg mL^{-1} was selected for subsequent in vitro experiments. 808-nm laser with power density of 1.0 W cm^{-2} was chosen for irradiation because this power density enables the nanoparticles to generate sufficient temperature elevation within 10 min to achieve tumor cell ablation, while simultaneously minimizing adverse effects such as skin burns at the irradiation site in subsequent in vivo experiments.

Cellular uptake of MPI NPs is critical for enhancing photothermal efficacy and multimodal imaging. To assess this mechanism, HeLa cells were incubated for 2 h with culture medium alone, free ICG, and MPI NPs. Nuclei were stained with Hoechst (blue), and CLSM was employed to obtain fluorescence images (Figure 3C). The colocalization analysis revealed significantly higher intracellular fluorescence intensity of MPI NPs than for free ICG and control group. Quantitative uptake was further assessed by flow cytometry (Figure S3). To validate the targeting capability and immune evasion properties conferred by the HeLa cell membranes coating, uptake efficiency of MPI NPs was compared among HeLa, H8, and RAW 264.7 cells by measuring ICG (red) fluorescence intensity (Figure 3D). Significantly greater uptake was observed in HeLa cells, confirming the effective tumor-targeting capacity of MPI NPs.[21]

The photothermal effect was further examined through live/dead cell staining. After NIR laser exposure, widespread cell death (PI staining, red, 545 nm) was observed in the MPI NPs + laser group, whereas other groups maintained good cell viability (calcein-AM staining, green, 488 nm) with only sporadic death (Figure 3E and F). Flow cytometry apoptosis assays (PE Annexin V/7-AAD double staining) showed pronounced accumulation of cells in the Q2 quadrant in the MPI NPs + laser group, consistent with substantial membrane injury, and concomitant membrane and nuclear staining (Figure 3G). Collectively, these results collectively demonstrated that MPI NPs possess favorable biocompatibility, tumor-targeting capability, and robust photothermal therapeutic efficacy, which are key to achieving integrated cancer theranostics.

In vivo Metabolism and Biosafety Evaluation

To further evaluate the in vivo stability of MPI NPs, a real-time metabolic tracking model was established within the NIR-I spectral window. Under 808-nm laser excitation, the biodistribution of MPI NPs was dynamically monitored in healthy mice using a in vivo NIR-I IVIS spectral imaging system. Mice were imaged under isoflurane anesthesia at 2, 8, 24, and 48 h post-injection. As shown in Figure S4, distinct NIR-I fluorescence signals from MPI NPs were detected in abdominal organs as early as 2 h post-administration, with the signal intensity peaking at 24 hours. This intense signal persisted through 48 h, indicating that the chemical stability of the liposomal framework combined with homologous camouflage by HeLa cell membranes synergistically suppressed fluorescence quenching and markedly prolonged circulation half-life.[44] At 48 h, mice were euthanized, and major organs (heart, liver, spleen, lung, and kidney) were collected for ex vivo fluorescence imaging and quantitative analysis. The results revealed predominant hepatic metabolism and renal excretion of MPI NPs, with only trace residual signal in the heart, spleen, and lungs, thereby confirming favorable in vivo distribution and controllable clearance.

Biocompatibility evaluation is an essential component of fundamental research, as it ensures biosafety and minimizes risk during biomedical applications. Before in vivo experiments in tumor-bearing model, hemolysis tests were performed and showed extremely minimal hemolysis at concentrations up to 200 μg mL^{-1} (Figure S5), indicating outstanding blood compatibility. Following intravenous injection of MPI NPs via the tail vein, blood samples were collected on Day 1, Day 7, and Day 14 for liver and kidney function tests and blood routine analysis (Figures 4A–F and S6). Hematological and

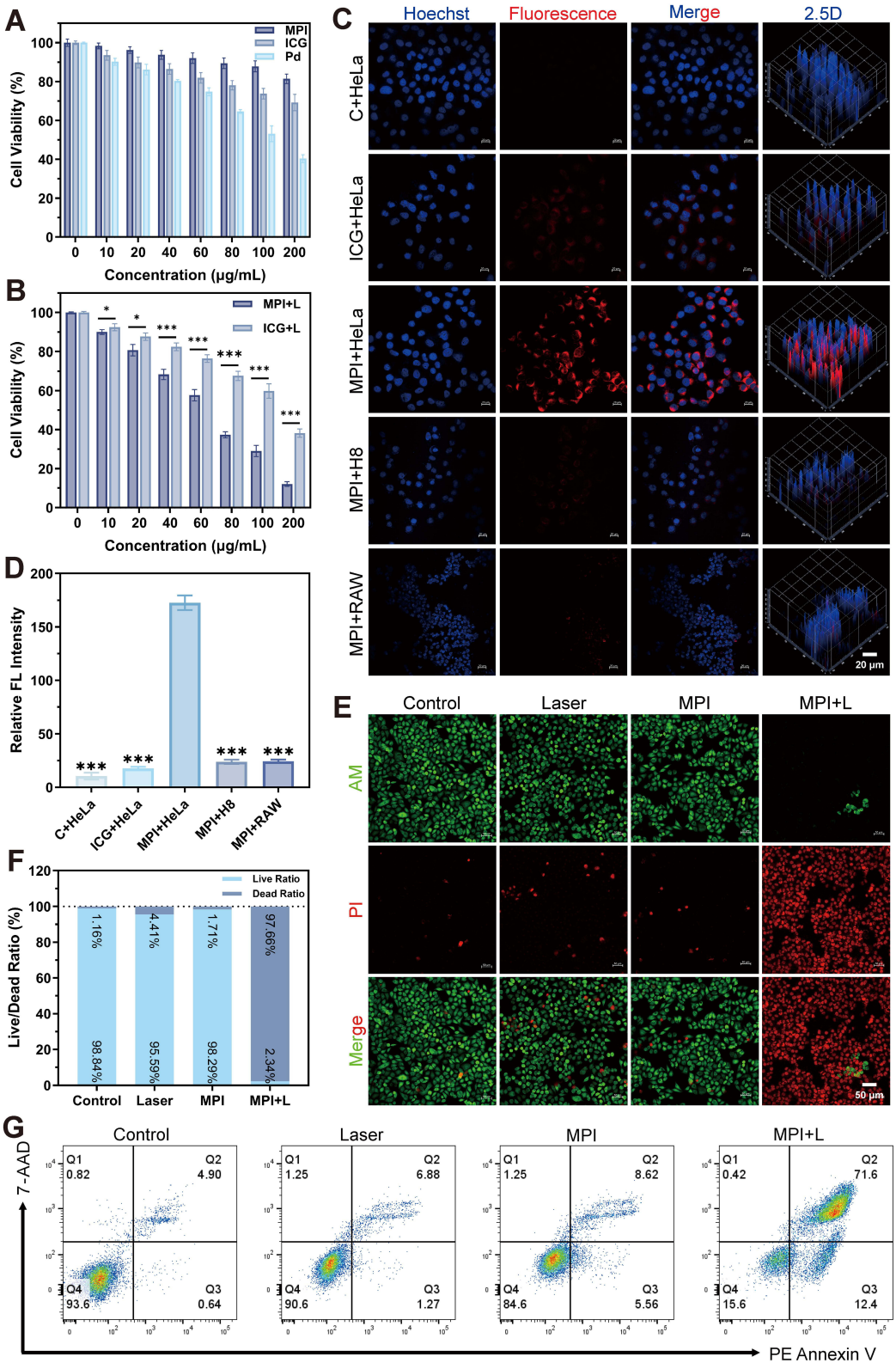

Figure 3 Cellular uptake and cytotoxicity of MPI NPs. (**A**) Dark toxicity analysis of Pd NPs, ICG, and MPI NPs on HeLa cells. (**B**) Phototoxicity analysis of ICG and MPI NPs on HeLa cells. (**C**) CLSM images of different cellular uptaking conditions (scale bar: 20 μm). (**D**) Quantitative analysis of fluorescence intensity under different cellular uptaking conditions. (**E**) Photothermal therapeutic efficacy evaluated by Calcein-AM/PI live-dead dual staining in HeLa cells (Laser: 808 nm, 1.0 W cm^{-2}; scale bar: 50 μm). (**F**) Quantitative analysis of live-dead cell CLSM imaging. (**G**) Flow cytometric analysis of HeLa cells apoptosis using PE Annexin V/7-AAD dual staining (Laser: 808 nm, 1.0 W cm^{-2}). Data are presented as mean values ± SD. *p < 0.05, and ***p < 0.001.

https://doi.org/10.2147/IJN.S576589

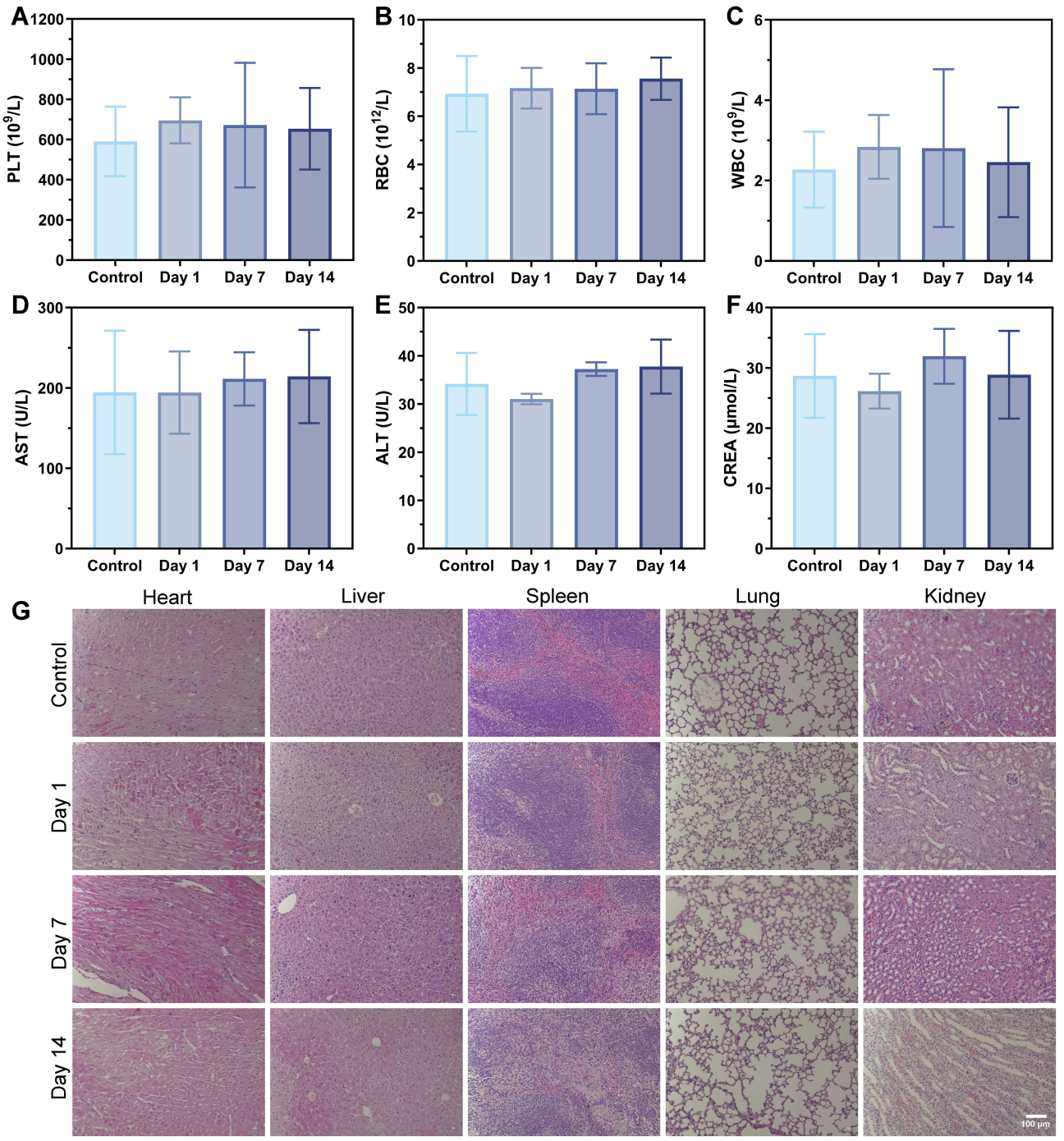

Figure 4 In vivo metabolism and biosafety of MPI NPs. (**A-F**) Toxicity assessment of MPI NPs in mice by monitoring changes in hematological and biochemical parameters (PLT, RBC, WBC, AST, ALT, CREA) at Day 1, Day 7, and Day 14 post-administration. (**G**) Analysis of microstructural damage in major organs by the H&E staining (scale bar: 100 μm). Data are presented as mean values ± SD.

serum biochemical tests (AST, ALT, TP, BUN, CREA, UA, HGB, WBC, RBC, PLT) were evaluated. Although slight fluctuations were observed, all values were broadly comparable to those of the control group, regardless of whether MPI NPs were administered for a short term (Day 1), medium term (Day 7), or long term (Day 14). Furthermore, H&E staining of major organs demonstrated no appreciable tissue damage or inflammatory infiltration (Figure 4G). In conclusion, MPI NPs exhibit favorable biocompatibility and biosafety.

https://doi.org/10.2147/IJN.S576589

In vivo Multimodal Imaging

To further characterize NPs distribution in tumor tissue, in vivo targeting experiments were conducted in the NIR-I and NIR-II spectral windows, utilizing the IVIS spectrum imaging system to assess the accumulation of MPI NPs (Figures 5A and S7). After intravenous injection of MPI NPs and PBS for 24 h, via the tails of CC-bearing mice, the fluorescence signal from the tumor region of the MPI NPs group was considerably enhanced compared to the control group (Figure 5B and C). Concurrently, experiments conducted by Ding et al[45] from our research group demonstrated that injection of ICG alone

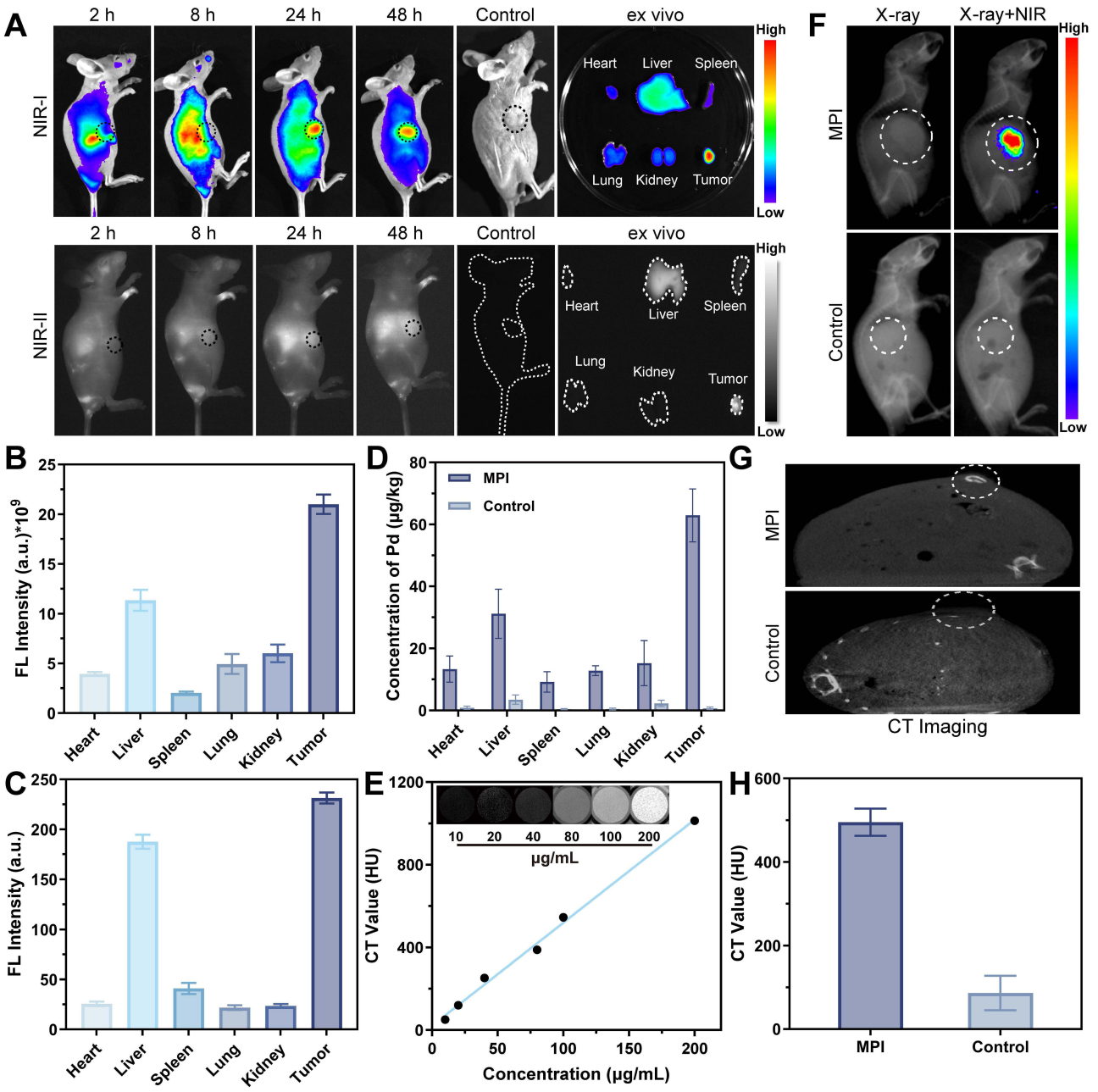

Figure 5 In vivo multimodal imaging of MPI NPs. (**A**) NIR-I and NIR-II fluorescence images of tumor sites at different times after tail vein injection of MPI NPs, corresponding fluorescence images of organs and tumors in 48 h (the black dashed line delineates the subcutaneous tumor region; the white dashed line outlines the body surface contour and the boundaries of the excised organs). (**B**) Quantitative analysis of fluorescence intensity (NIR-I) in ex vivo organs and tumors at 48 h. (**C**) Quantitative analysis of fluorescence intensity (NIR-II) in ex vivo organs and tumors at 48 h. (**D**) ICP-MS analysis of Pd content in organs and tumors at 48 h. (**E**) CT imaging of MPI NPs dispersion at different concentrations and the functional relationship between MPI NPs concentrations and CT values. (**F**) Dual-modal in vivo imaging integrating X-ray imaging and NIR-I fluorescence imaging (the white dashed line delineates the subcutaneous tumor region). (**G**) CT imaging of the tumor sites (the white dashed line delineates the subcutaneous tumor region). (**H**) CT values of the tumor sites. Data are presented as mean values ± SD.

https://doi.org/10.2147/IJN.S576589

resulted in weak fluorescence and short accumulation duration at the tumor site, confirming the robust tumor targeting and accumulation capabilities of MPI NPs. Dual validation demonstrated that the active targeting strategy employing HeLa cell membranes can mediate greater internalization of MPI NPs by tumor cells, facilitating in vivo tumor localization and tracking. Tumor accumulation of Pd was subsequently quantified by ICP-MS analysis, revealing significantly higher Pd content in tumor tissue relative to other organs (Figure 5D). These results indicate that the HeLa cell membranes modification strategy enables NPs to evade immune clearance and prolong in vivo circulation.

Leveraging the X-ray imaging property of MPI NPs, micro-CT was employed to further investigate the CT imaging effects of MPI NPs both in vitro and in vivo. A concentration-dependent increase in Hounsfield unit (HU) values was observed with rising MPI NPs concentration (Figure 5E), confirming dose-dependent X-ray absorption property and establishing theoretical basis for application as CT contrast agents.

To comprehensively estimate the multimodal imaging performance of MPI NPs, synchronized NIR fluorescence and X-ray images were acquired in CC-bearing mice and overlaid (Figure 5F). The tumor region exhibited both high-intensity NIR fluorescence and high-density X-ray shadows, forming a "double-high" feature. This achievement validated the feasibility of combining high spatiotemporal resolution NIRFI with high-penetration X-ray imaging at the animal experimental level, providing a solid foundation for detailed observation, longitudinal comparison, and quantitative analysis in CC imaging diagnosis, with the potential to significantly improve diagnostic accuracy and reliability. Furthermore, in vivo CT experiments (Figure 5G) showed that tumor sites of mice injected with MPI NPs displayed markedly increased attenuation, with significantly higher HU values than the control group (Figure 5H).

From the perspective of NPs design, this structure achieves complementary advantages through functional integration: the HeLa cell membranes confer homologous targeting and immune evasion capabilities; the high atomic number Pd NPs provide strong CT contrast and efficient photothermal conversion, while ICG complements the system with a highly sensitive optical imaging dimension. This integrated strategy not only significantly enhances the precision of lesion localization but also lays the foundation for the visualization of subsequent PTT.

In vivo Evaluation of Photothermal Therapy

Figure 6A illustrates the experimental flowchart of the in vivo antitumor study. Given their excellent biosafety and targeting properties, NIR thermography was used to capture temperature variations and photothermal images under laser irradiation. Mice were injected with PBS and MPI NPs via the tail vein, respectively, and then exposed to 808-nm laser irradiation (1.0 W cm^{-2}) 24 h later. In PTI (Figure 6B), tumor regions of the MPI NPs group exhibited significantly elevated temperatures compared with surrounding tissues after laser exposure, fully demonstrating the integrated advantages of MPI NPs in tumor specific localization and photothermal effect triggering. As shown in Figure 6C, the tumor temperature in the PBS group remained largely unchanged, the tumor region in the MPI NPs group reached 48.0 °C within 5 min, indicating that the NPs can serve as efficient photothermal agent by converting laser energy into thermal energy under laser irradiation and meeting the conditions for effective tumor PTT.[46] By monitoring temperature distribution changes in the tumor region under laser irradiation, the accumulation and photothermal conversion efficiency of MPI NPs were intuitively reflected, providing visual guidance for potential PTT.

To further investigate the in vivo antitumor effects, a CC-bearing BALB/c nude mouse model was employed. Tumor-bearing mice were randomly divided into four groups, and tumor growth was monitored for 15 days post-intervention to evaluate the efficacy of PTT. Tumor tissues were harvested from euthanized mice and weighed (Figure 6D), demonstrating that the tumor mass in the MPI NPs + laser combination therapy group was noticeably lower than that in the other three groups (Figure 6E). Throughout the observation period, only the MPI NPs + laser group demonstrated a progressive reduction in tumor weight (Figure 6F), achieving a tumor inhibition rate of 85% (Figure S8). Furthermore, Figure 6G showed no significant changes in average body weight throughout treatment, suggesting that the NPs formulation, laser irradiation, and tumor model induced minimal adverse effects on the animals. After observation, main organs and tumor tissues of the mice were harvested and processed for H&E histology. No obvious organ damage or inflammation was observed (Figure S9). As shown in Figure 6H, the TUNEL assay revealed the most intense green fluorescence in the combination group, reflecting extensive cellular apoptosis.

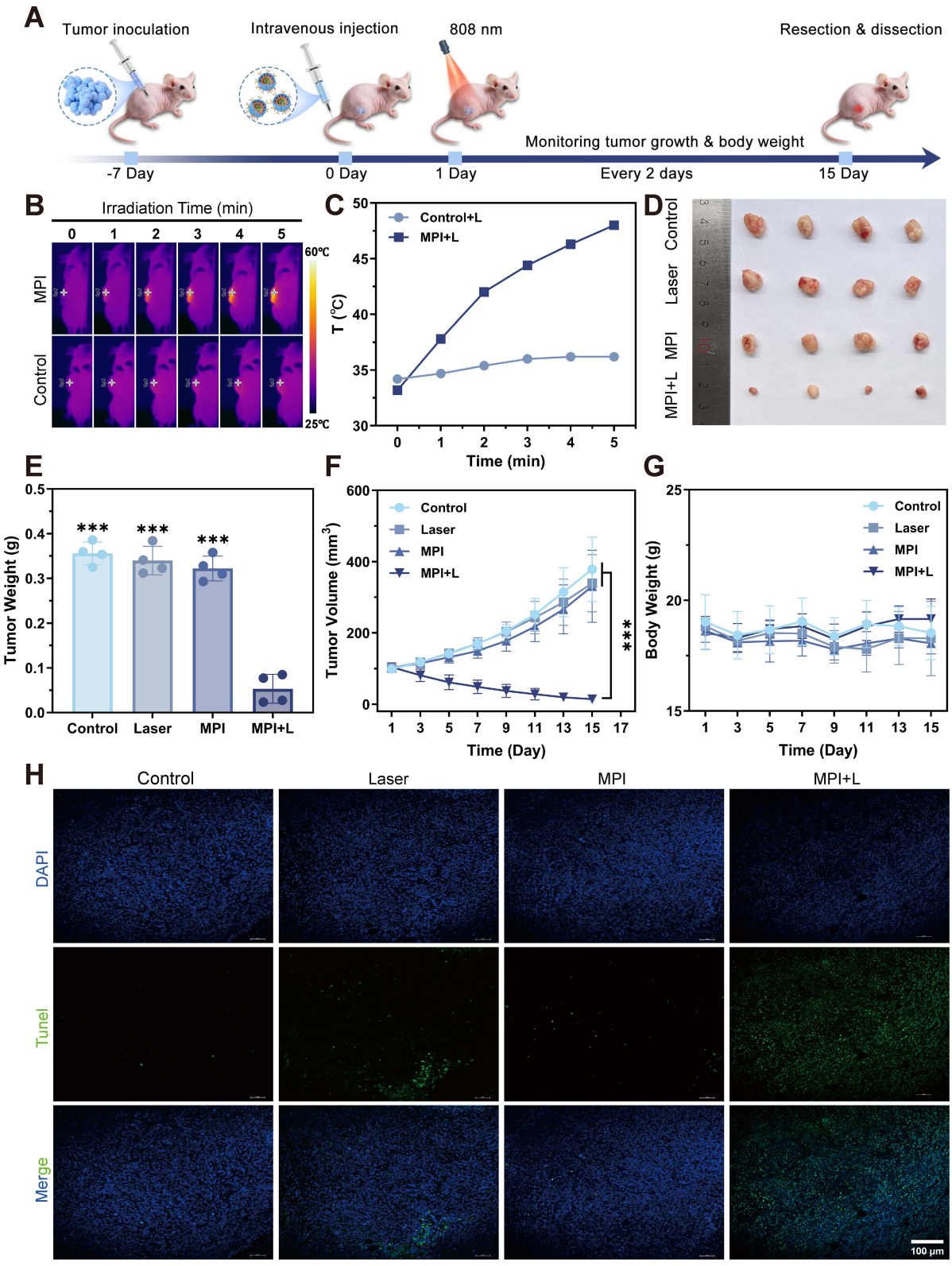

Figure 6 In vivo treatment with MPI NPs in the mouse tumor model. (**A**) Treatment scheme for MPI NPs in the mouse tumor model. (**B**) Infrared imaging of cervical tumor-bearing mice after 808-nm laser irradiation (1.0 W/cm^2, 5 min). (**C**) Photothermal temperature curves at various time points. (**D**) Tumor images across different treatment groups (n=4). (**E**) Tumor weight of excised tumors across different treatment groups. (**F**) Tumor growth curves across different treatment groups. (**G**) Body weight curves of tumor-bearing mice across various treatment groups over time. (**H**) TUNEL fluorescence staining images of tumor tissues across different treatment groups (scale bar: 100 μm). Data are presented as mean values ± SD. ***$p < 0.001$.

https://doi.org/10.2147/IJN.S576589

These findings demonstrated that HeLa cell membranes coating significantly enhances tumor cell uptake of MPI NPs. Under a single 808-nm NIR laser irradiation, ICG and Pd NPs embedded in the NPs synergistically and efficiently convert laser energy into thermal energy, thereby amplifying the PTT effect. Furthermore, integrating targeted multimodal imaging with PTT into a single nanoplatform provides an innovative synergistic strategy for further biomedical applications.

Conclusion

In summary, a novel type of biomimetic multifunctional theranostic nanoplatform (M@Pd-ICG NPs) was integrated multimodal imaging with PTT for precise diagnosis and treatment of CC in this study. The results demonstrated that MPI NPs effectively achieved multimodal imaging, while concurrently exerting pronounced antitumor effects, which are crucial for the development of integrated theranostic nanoplatforms. Specifically, the tumor cell membranes coating not only significantly prolonged in vivo circulation and reduced the immune clearance but also enhanced tumor site accumulation through homologous targeting, thereby ensuring sustained imaging and therapeutic effects. Pd NPs and ICG were co-encapsulated to enable synergistic photothermal efficacy and to provide complementary imaging contrast: Pd NPs afforded strong X-ray attenuation for CT, whereas ICG supplied optical signals for NIRFI and PTI. In terms of multimodal imaging, the time point at which the most significant tumor signal was observed via NIRFI at 24 h post-injection was selected as the irradiation window. The anatomical localization and contrast enhancement of the tumor site were confirmed by CT. Subsequently, during irradiation, PTI was employed to monitor the temperature rise in real time, ensuring that the therapeutic threshold was reached while controlling the risk of thermal diffusion. This approach demonstrates the complementary synergy of the three modalities within a single therapeutic workflow. Regarding tumor treatment, MPI NPs demonstrated outstanding PCE under 808-nm laser irradiation, rapidly generating heat and effectively ablating CC tumors, yielding significant tumor suppression with a single irradiation. Overall, MPI NPs combine biomimetic tumor cell membranes modification with multi-component synergistic design, balancing efficient and safe imaging functionality with remarkable photothermal therapeutic efficacy. This study provides an innovative strategy for imaging and therapy of CC.

Funding

This work was supported by the National Natural Science Foundation of China (Nos. 82260613, 82073475, 52250007, 62035011, 82202220 and 82060326), State Key Laboratory of Pathogenesis, Prevention and Treatment of High Incidence Diseases in Central Asia Key Project (Nos. SKL-HIDCA-2024-3 and SKL-HIDCA-2024-GJ9), Xinjiang Uygur Autonomous Region Natural Science Foundation Outstanding Youth Project (No. 2023D01E06), Key Project (No. 2022D01D40), Youth Science Fund (No. 2022D01C715), Tianshan Talent Program for High-Level Medical and Health Professionals (No. TSYC202401B016), Central Guidance for Local Science and Technology Development Special Program (No. ZYYD2023A09), and Xinjiang Uygur Autonomous Region Regional Collaborative Innovation Special Science and Technology Assistance Program (No. 2022E02130).

Disclosure

The authors report no conflicts of interest in this work.

References

1. Bray F, Laversanne M, Sung H, et al. Global cancer statistics 2022: GLOBOCAN estimates of incidence and mortality worldwide for 36 cancers in 185 countries. *Ca Cancer J Clin*. 2024;74(3):229–263. doi:10.3322/caac.21834
2. Xu M, Cao C, Wu P, Huang X, Ma D. Advances in cervical cancer: current insights and future directions. *Cancer Commun*. 2025;45(2):77–109. doi:10.1002/cac2.12629
3. Deo SVS, Sharma J, Kumar S. GLOBOCAN 2020 report on global cancer burden: challenges and opportunities for surgical oncologists. *Ann Surg Oncol*. 2022;29(11):6497–6500. doi:10.1245/s10434-022-12151-6
4. World Health Organization. Cervical cancer: key facts; 2024. Available from: https://www.who.int/news-room/fact-sheets/detail/cervical-cancer. Accessed March 17, 2026.
5. Fischerova D, Frühauf F, Burgetova A, Haldorsen IS, Gatti E, Cibula D. The role of imaging in cervical cancer staging: ESGO/ESTRO/ESP guidelines (update 2023). *Cancers*. 2024;16(4):775.

6. Jackson A, Pathak R, deSouza NM, et al. MRI apparent diffusion coefficient (ADC) as a biomarker of tumour response: imaging-pathology correlation in patients with hepatic metastases from colorectal cancer (EORTC 1423). *Cancers*. 2023;15(14):3580. doi:10.3390/cancers15143580
7. Zhu L, Jiang Y, Tian H, et al. Recent advancement in MRI-based nanotheranostic agents for tumor diagnosis and therapy integration. *Int J Nanomed*. 2025;20:10503–10540. doi:10.2147/IJN.S529003
8. Jiang Z, Zhang M, Li P, Wang Y, Fu Q. Nanomaterial-based CT contrast agents and their applications in image-guided therapy. *Theranostics*. 2023;13(2):483–509. doi:10.7150/thno.79625
9. Zhang M, Zhang Y, Hang L, et al. Bionic nanotheranostic for multimodal imaging-guided NIR-II-photothermal cancer therapy. *Nanoscale*. 2024;16 (12):6095–6108. doi:10.1039/d4nr00230j
10. Zhu L, Du Z, Xiong J, et al. Phototheranostic LPP-QDs-IR-820 nanocomposites for specific NIR-II imaging of lymphatic and photothermal therapy of cervical tumors. *Adv Healthcare Materials*. 2024;13(29):2401358. doi:10.1002/adhm.202401358
11. Yang C, Che X, Zhang Y, et al. Hybrid FeWO4-Hyaluronic acid nanoparticles as a targeted nanotheranostic agent for multimodal imaging-guided tumor photothermal therapy. *Int J Nanomed*. 2023;18:8023–8037. doi:10.2147/IJN.S432533
12. Zheng F, Huang X, Ding J, et al. NIR-I dye-based probe: a new window for bimodal tumor theranostics. *Front Chem*. 2022;10:859948. doi:10.3389/fchem.2022.859948
13. Du Z, Ma R, Chen S, et al. A highly efficient polydopamine encapsulated clinical ICG theranostic nanoplatform for enhanced photothermal therapy of cervical cancer. *Nanoscale Adv*. 2022;4(18):4016–4024. doi:10.1039/D2NA00341D
14. Sevieri M, Silva F, Bonizzi A, et al. Indocyanine green nanoparticles: are they compelling for cancer treatment? *Front Chem*. 2020;8:535. doi:10.3389/fchem.2020.00535
15. Tomar A, Stern N, Porter T, Dunn AK. Improving vascular retention of indocyanine green for in vivo two-photon microscopy using liposomal encapsulation. *J Biomed Opt*. 2025;30(09). doi:10.1117/1.JBO.30.9.096004
16. De Leo V, Maurelli AM, Giotta L, Catucci L. Liposomes containing nanoparticles: preparation and applications. *Colloids Surf B*. 2022;218:112737. doi:10.1016/j.colsurfb.2022.112737
17. Ahmad MY, Liu S, Tegafaw T, et al. Heavy metal-based nanoparticles as high-performance X-ray computed tomography contrast agents. *Pharmaceuticals*. 2023;16(10):1463. doi:10.3390/ph16101463
18. Zhang W, Li J, Chen L, Chen H, Zhang L. Palladium-based multifunctional nanoparticles for combined chemodynamic/photothermal and calcium overload therapy of tumors. *Colloids Surf B*. 2023;230:113529. doi:10.1016/j.colsurfb.2023.113529
19. FitzGerald PF, Colborn RE, Edic PM, et al. CT image contrast of high- *Z* elements: phantom imaging studies and clinical implications. *Radiology*. 2016;278(3):723–733. doi:10.1148/radiol.2015150577
20. Stribbling SM, Ryan AJ. The cell-line-derived subcutaneous tumor model in preclinical cancer research. *Nat Protoc*. 2022;17(9):2108–2128. doi:10.1038/s41596-022-00709-3
21. Zhao Y, Wen M, Yu N, et al. Design and synthesis of cancer-cell-membrane-camouflaged hemoporfin-Cu9S8 nanoagents for homologous tumor-targeted photothermal-sonodynamic therapy. *J Colloid Interface Sci*. 2023;637:225–236. doi:10.1016/j.jcis.2023.01.068
22. Li SY, Cheng H, Qiu WX, et al. Cancer cell membrane-coated biomimetic platform for tumor targeted photodynamic therapy and hypoxia-amplified bioreductive therapy. *Biomaterials*. 2017;142:149–161. doi:10.1016/j.biomaterials.2017.07.026
23. Guo Q, Wang S, Xu R, Tang Y, Xia X. Cancer cell membrane-coated nanoparticles: a promising anti-tumor bionic platform. *RSC Adv*. 2024;14 (15):10608–10637. doi:10.1039/d4ra01026d
24. Chen Y, Zhi S, Ou J, et al. Cancer cell membrane-coated nanoparticle co-loaded with photosensitizer and toll-like receptor 7 agonist for the enhancement of combined tumor immunotherapy. *ACS Nano*. 2023;17(17):16620–16632. doi:10.1021/acsnano.3c02724
25. Faustino-Rocha A, Oliveira PA, Pinho-Oliveira J, et al. Estimation of rat mammary tumor volume using caliper and ultrasonography measurements. *Lab Anim*. 2013;42(6):217–224. doi:10.1038/laban.254
26. Wang L, Zhang D, Li J, et al. A novel ICG-labeled cyclic TMTP1 peptide dimer for sensitive tumor imaging and enhanced photothermal therapy in vivo. *Eur J Med Chem*. 2022;227:113935. doi:10.1016/j.ejmech.2021.113935
27. Karamboulas C, Meens J, Ailles L. Establishment and use of patient-derived xenograft models for drug testing in head and neck squamous cell carcinoma. *STAR Protocols*. 2020;1(1):100024. doi:10.1016/j.xpro.2020.100024
28. Swatler J, Targońska A, Turos-Korgul L, Mosieniak G, Piwocka K. Protocol for isolation of tumor-derived extracellular vesicles and functional studies on human T cell subsets. *Star Protoc*. 2024;5(2):103011. doi:10.1016/j.xpro.2024.103011
29. Anila PA, Keerthiga B, Ramesh M, Muralisankar T. Synthesis and characterization of palladium nanoparticles by chemical and green methods: a comparative study on hepatic toxicity using zebrafish as an animal model. *Comp Biochem Physiol C*. 2021;244:108979. doi:10.1016/j.cbpc.2021.108979
30. Wrasman CJ, Boubnov A, Riscoe AR, Hoffman AS, Bare SR, Cargnello M. Synthesis of colloidal pd/au dilute alloy nanocrystals and their potential for selective catalytic oxidations. *J Am Chem Soc*. 2018;140(40):12930–12939. doi:10.1021/jacs.8b07515
31. Choi J, Kim G, Park B, et al. Theranostic gold nanoparticles encapsulated in a PEGylated liposome as an effective radiosensitizer for cancer radiation therapy. *ACS Appl Bio Mater*. 2025;8(9):7877–7888. doi:10.1021/acsabm.5c00908
32. Wu C, Sun Q, Liu X, Sun X, Chen Z, Shan H. Indocyanine green-loaded liposomes-assisted photoacoustic computed tomography for evaluating in vivo tumor penetration of liposomal nanocarriers. *Micromachines*. 2023;15(1):90. doi:10.3390/mi15010090
33. Srivastava I, Lew B, Wang Y, et al. Cell-membrane coated nanoparticles for tumor delineation and qualitative estimation of cancer biomarkers at single wavelength excitation in murine and phantom models. *ACS Nano*. 2023;17(9):8465–8482. doi:10.1021/acsnano.3c00578
34. Ma R, Alifu N, Du Z, et al. Indocyanine Green-Based theranostic nanoplatform for NIR fluorescence Image-Guided Chemo/Photothermal therapy of cervical cancer. *Int J Nanomed*. 2021;16:4847–4861. doi:10.2147/IJN.S318678
35. Wang C, Zhou L, Liu C, et al. Pt nanoshells with a high NIR-II photothermal conversion efficiency mediates multimodal neuromodulation against ventricular arrhythmias. *Nat Commun*. 2024;15(1):6362. doi:10.1038/s41467-024-50557-w
36. Fan H, Chen S, Du Z, et al. New indocyanine green therapeutic fluorescence nanoprobes assisted high-efficient photothermal therapy for cervical cancer. *Dyes Pigm*. 2022;200:110174. doi:10.1016/j.dyepig.2022.110174
37. Yang Y, Liu Q, Wang M, et al. Genetically programmable cell membrane-camouflaged nanoparticles for targeted combination therapy of colorectal cancer. *Signal Transduction Targeted Ther*. 2024;9(1):158. doi:10.1038/s41392-024-01859-4
38. Cho J, Nouizi F, Kim CS, Gulsen G. Monitoring distribution of the therapeutic agent dimethyl sulfoxide via solvatochromic shift of albumin-bound indocyanine green. *Sens*. 2023;23(18):7728. doi:10.3390/s23187728

39. Zhou J, Li H, Li H, et al. Constructing J-aggregates of cyanine dye for NIR-II in vivo dynamic vascular imaging and long-term targeting of tumors. *Mater Today Bio*. 2025;32:101693. doi:10.1016/j.mtbio.2025.101693
40. Chen C, Huang Y, Wang W, et al. An anisotropic gold-palladium heterostructured nanosystem for synergistically overcoming radioresistance and enhancing melanoma radioimmunotherapy. *Adv Sci*. 2025. doi:10.1002/advs.202500492
41. George BP, Chota A, Sarbadhikary P, Abrahamse H. Fundamentals and applications of metal nanoparticle- enhanced singlet oxygen generation for improved cancer photodynamic therapy. *Front Chem*. 2022;10:964674. doi:10.3389/fchem.2022.964674
42. Feng G, Zhang GQ, Ding D. Design of superior phototheranostic agents guided by jablonski diagrams. *Chem Soc Rev*. 2020;49(22):8179–8234. doi:10.1039/D0CS00671H
43. Zhong Z, Deng W, Wu J, et al. Cell membrane coated nanoparticles as a biomimetic drug delivery platform for enhancing cancer immunotherapy. *Nanoscale*. 2024;16(18):8708–8738. doi:10.1039/d4nr00284a
44. Zhang S, Zhang X, Gao H, et al. Cell membrane-coated biomimetic nanoparticles in cancer treatment. *Pharmaceutics*. 2024;16(4):531. doi:10.3390/pharmaceutics16040531
45. Ding J, Zhang X, Guo L, et al. NIR triggered bionic bilayer membrane-encapsulated nanoparticles for synergistic photodynamic, photothermal and chemotherapy of cervical cancer. *Int J Nanomed*. 2025;20:141–159. doi:10.2147/ijn.s496982
46. Cuadrado CF, Lagos KJ, Stringasci MD, Bagnato VS, Romero MP. Clinical and pre-clinical advances in the PDT/PTT strategy for diagnosis and treatment of cancer. *Photodiagn Photodyn Ther*. 2024;50:104387. doi:10.1016/j.pdpdt.2024.104387